

One-dimensional electron-phonon systems: Mott- versus Peierls-insulators

H. Fehske^{1,2}, G. Wellein³, A. P. Kampf⁴, M. Sekania⁴, G. Hager³,
A. Weiße², H. Büttner², and A. R. Bishop⁵

¹ Institut für Physik, Universität Greifswald, 17487 Greifswald

² Physikalisches Institut, Universität Bayreuth, 95440 Bayreuth

³ Regionales Rechenzentrum Erlangen, Universität Erlangen, 91058 Erlangen

⁴ Institut für Physik, Universität Augsburg, 86135 Augsburg

⁵ Theoretical Division and Center for Nonlinear Studies, Los Alamos National
Laboratory, Los Alamos, New Mexico 87545, U.S.A.

Summary. We analyze ground state and spectral properties of the one-dimensional half-filled Holstein Hubbard model with respect to the Peierls-insulator to Mott-insulator transition, exploiting Lanczos diagonalization, density matrix renormalization, kernel polynomial expansion, and maximum entropy methods on the Hitachi SR8000-F1 supercomputer.

1 Introduction

Quasi-one-dimensional (1D) strongly coupled electron-phonon systems like MX-chain compounds or conjugated polymers are particularly rewarding to study for a number of reasons. They exhibit a remarkable wide range of strengths of competing forces and, as a result, physical properties. These systems share fundamental features with higher dimensional novel materials, such as high-temperature superconductors, charge-ordered nickelates or colossal magneto-resistance manganites, i.e., they are complex enough to investigate the interplay of charge, spin, and lattice degrees of freedom which is important for strongly correlated electronic systems in two and three dimensions as well. Nevertheless they are simple enough to allow for a nearly microscopic modeling. Thus they are suited modern systems to develop and test new theoretical methods by bringing together techniques from quantum chemistry, electronic band structure investigations, and many-body physics.

Two properties of quasi-1D materials are crucial for their unusual electronic, magnetic and optical properties: first they have broken-symmetry ground states, and second, in the insulating phases, they have gap states. The first feature arises, because the itinerancy of the electrons strongly competes with electron-electron and electron-phonon (EP) interactions, which tend to localize the charge carriers by establishing spin-density-wave (SDW) and charge-density-wave (CDW) ground states, respectively. Hence, at half-filling, Mott (MI) or Peierls (PI) insulating phases are energetically favored over the

metallic state. An interesting and still controversial question is whether or not only one quantum critical point separates the PI and MI phases at temperature $T = 0$ [2]. The second feature, i.e. the existence of gap states, may be caused by donating electrons to or accepting electrons from the half-filled host material. Those charged gap states are related to local lattice distortions (polarons or bipolarons). Another possibility is “photo-doping”, i.e. the creation of neutral excitations (e.g., excitons). More recently, the existence and stability of intrinsically localized vibrational modes has been demonstrated both experimentally and theoretically in clean strong-CDW MX-materials [3]. These multi-phonon bound states occur inside the CDW gap when the effective lattice potential, dynamically self-generated in the process of carrier localization, exhibits a significant nonlinearity as a consequence of a non-adiabatic electron-phonon interaction of intermediate strength.

Significant progress has been made towards understanding the physics underlying these various effects by numerical investigations of generic model Hamiltonians. Neglecting in a first step the lattice dynamics, a frequently used starting point has been the *adiabatic Holstein-Hubbard model* (AHHM):

$$H_{AHHM} = H_{t-U} - \sum_{i,\sigma} \Delta_i n_{i\sigma} + \frac{\kappa}{2} \sum_i \Delta_i^2, \quad (1)$$

$$H_{t-U} = -t \sum_{i,\sigma} (c_{i\sigma}^\dagger c_{i+1\sigma} + \text{H.c.}) + U \sum_i n_{i\uparrow} n_{i\downarrow}. \quad (2)$$

Here, H_{t-U} constitutes the conventional Hubbard Hamiltonian with hopping amplitude t and on-site Coulomb repulsion strength U ; $c_{i\sigma}^\dagger$ creates a spin- σ electron at Wannier site i and $n_{i\sigma} = c_{i\sigma}^\dagger c_{i\sigma}$. In addition, H_{AHHM} includes the elastic energy of a harmonic lattice with a “spring constant” κ . Within this so-called frozen phonon approach, $\Delta_i = (-1)^i \Delta$ is a measure of the static, staggered density modulations of the PI phase. Eq. (1) with $\kappa = 0$ and fixed Δ is known as the ionic Hubbard model (IHM) for which a band insulator (BI) to MI transition has been established previously [2]. The BI-MI transition of the IHM on finite lattices was shown to be connected to a ground state level crossing with a site-parity change, where the site inversion symmetry operator P is defined by $P c_{i\sigma}^\dagger P^\dagger = c_{N-i\sigma}^\dagger$ with $N = 4n$ [4].

Of course, dynamical phonon effects are known to be particularly important in quasi-1D materials, where the lattice zero-point motion is usually comparable to the Peierls distortion [5]. By any means quantum phonon effects should be included in a theoretical analysis of transport and optical properties of electronically 1D compounds. Introducing phonon creation b_i^\dagger and destruction operators b_i , the general *Holstein-Hubbard Hamiltonian* (HHM) takes the form

$$H = H_{t-U} - g\omega_0 \sum_{i,\sigma} (b_i^\dagger + b_i) n_{i\sigma} + \omega_0 \sum_i b_i^\dagger b_i, \quad (3)$$

where $g = \sqrt{\varepsilon_p/\omega_0}$ is a dimensionless EP coupling constant and ω_0 denotes the frequency of the optical phonon mode. The physics of the HHM is governed by three competing effects: the itinerancy of the electrons, their Coulomb repulsion and the local EP interaction. There are two dimensionless energy ratios, U/t and ε_p/t , which determine the tendency of the itinerant quantum mechanical system to establish a magnetic or charge ordered state, respectively. Since the EP coupling is retarded, the phonon frequency ω_0 defines a third relevant energy scale of the problem. At $U = 0$, the ground state of the pure half-filled Holstein model is a Peierls distorted state with staggered charge order in the adiabatic limit $\omega_0 \rightarrow 0$ for any finite ε_p . However, as in the HM of spinless fermions, quantum phonon fluctuations destroy the Peierls state for small EP interaction strength [6]. Above a critical threshold $g_c(\omega_0)$, the HM describes a PI with equal spin (Δ_s) and charge (Δ_c) excitation gaps – the characteristic feature of a band insulator.

In what follows, exact numerical methods [7] are used to diagonalize the HHM on finite chains, preserving the full dynamics of the phonons, and the density matrix renormalization group (DMRG) technique is applied to the AHHM and IHM.

2 Peierls- to Mott-insulator transition

In order to draw conclusions about the phase diagram in the *adiabatic limit*, we plot in Fig. 1 $\Delta(U, \kappa)$ obtained from DMRG on an open chain of length $N = 64$, where the value for the stiffness constant is fixed at $\kappa = 0.74$. In contrast to the behavior of the 8-site chain $\Delta(U, \kappa)$ decreases more smoothly with increasing U and vanishes discontinuously near $U/2\varepsilon_p \approx 0.75$. Also shown in Fig. 1 is the level crossing line $\Delta_{cr}(U)$ of the IHM obtained from finite-size scaling of Lanczos results for rings of up to 14 sites; $\Delta_{cr}(U)$ remains finite in the infinite chain length limit. Importantly, $\Delta(U, \kappa)$ and $\Delta_{cr}(U)$ do not intercept because $\Delta(U, \kappa)$ jumps to zero before reaching the level

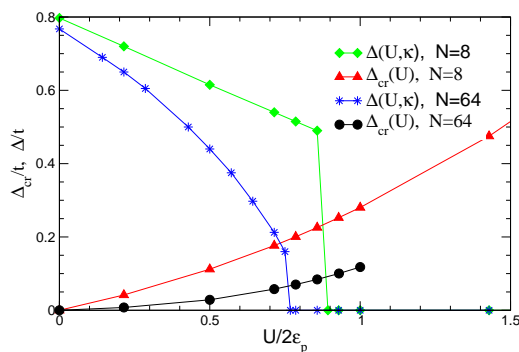


Fig. 1. Level crossing line $\Delta_{cr}(U)$ of the IHM for an 8-site ring (red triangles) and from finite-size scaling (black circles). In addition: ionic potential strength $\Delta(U, \kappa)$ of the AHHM for an 8-site ring (green diamonds) and on an open 64-site chain (blue stars).

crossing point of the IHM. The discontinuous nature of the PI-MI transition in the AHHM is easily verified in the atomic limit $t = 0$ where $\Delta = 1/\kappa$ for $U < U_c = 1/\kappa$ and $\Delta = 0$ for $U > U_c$. The first order nature persists for finite small t , i.e. in the strong coupling regime $U, \kappa^{-1} \gg t$. However, as we have explicitly verified by diagonalization of a periodic AHHM ring of length $N = 14$, the transition is second order in the weak coupling regime $U, \kappa^{-1} \ll t$. This implies a continuous decrease of $\Delta(U)$ and therefore $\Delta(U)$ necessarily intercepts the $\Delta_{cr}(U)$ line of the IHM (c.f. Fig. 3). This intercept marks the point U_{opt} when the site-parity sectors become degenerate and the optical absorption gap Δ_{opt} disappears. For weak coupling the PI-MI transition therefore evolves across *two* critical points. We summarize these findings in the phase diagram shown in Fig. 2. In the Peierls BI phase for $U < U_{opt}$ the spin and charge excitation gaps are equal and finite, and remarkably $\Delta_{opt} \neq \Delta_c$ [8]. When the site-parity sectors become degenerate at $U = U_{opt}$, $\Delta_{opt} = 0$ but $\Delta_c = \Delta_s > 0$. For $U \geq U_s$ the usual MI phase with $\Delta_{opt} = \Delta_c > \Delta_s = 0$ is realized. For strong coupling $U_{opt} = U_s$ holds. In weak coupling there exists an intermediate region $U_{opt} < U < U_s$ in which all excitation gaps are finite. The CDW persists for all $U < U_s$. The site-parity eigenvalue is $P = +1$ in the PI and $P = -1$ in the MI phase. It is natural to expect an additional ordering phenomenon in the window $U_{opt} < U < U_s$.

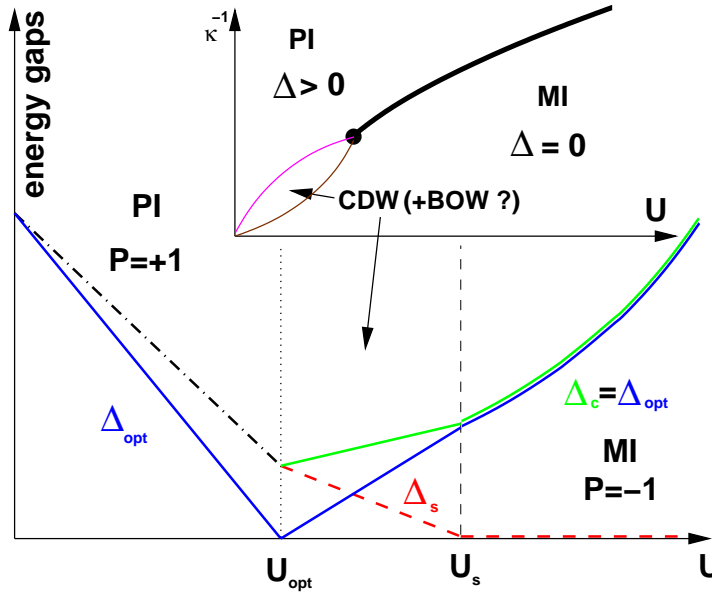


Fig. 2. Qualitative phase diagram of the AHHM. Inset: Transition scenario in the weak coupling regime $U, \kappa^{-1} \ll t$.

A bond order wave (BOW) with a finite expectation value of the staggered bond charge $B = \frac{1}{N} \sum_{i\sigma} (-1)^i \langle c_{i\sigma}^\dagger c_{i+1\sigma} + \text{H.c.} \rangle$ is the natural candidate.

In order to discuss the PI-MI transition at finite phonon frequencies, i.e. in the *non-adiabatic regime*, we have calculated the regular part of the optical conductivity at $T = 0$,

$$\sigma^{reg}(\omega) = \frac{\pi}{N} \sum_{m \neq 0} \frac{|\langle \psi_0 | \hat{j} | \psi_m \rangle|^2}{E_m - E_0} \delta(\omega - E_m + E_0). \quad (4)$$

Here $|\psi_0\rangle$ and $|\psi_m\rangle$ denote the ground state and excited states, respectively, with corresponding energies E_0 and E_m . Note that the current operator $\hat{j} = -iet \sum_{i\sigma} (c_{i\sigma}^\dagger c_{i+1\sigma} - c_{i+1\sigma}^\dagger c_{i\sigma})$ has finite matrix elements between states of different site-parity only.

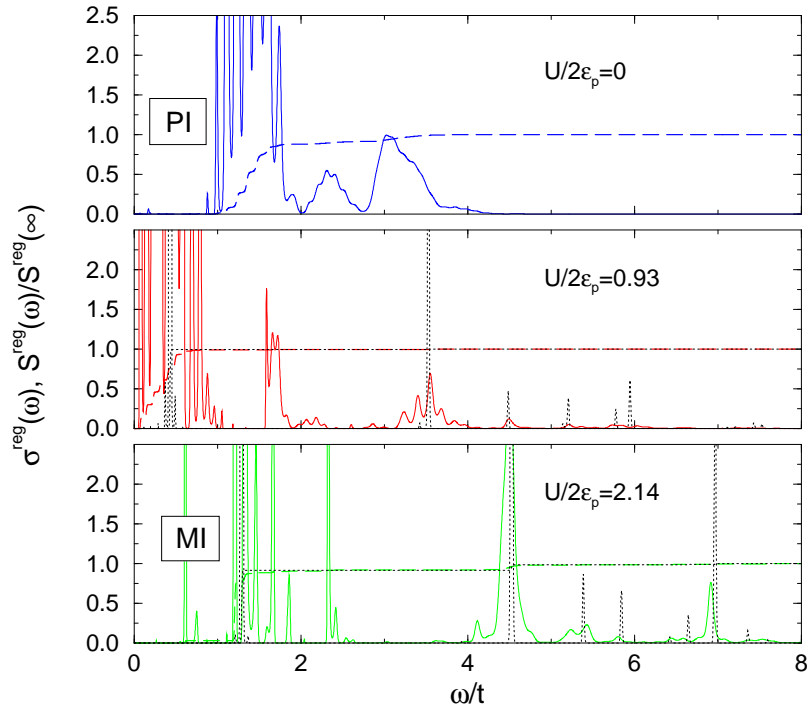


Fig. 3. Optical conductivity in the 8-site HHM ring for $\omega_0 = 0.1t$ and $g^2 = 7$. Top panel: PI phase for $U = 0$; middle panel: near criticality $U \sim U_{opt}$; lower panel: MI phase for $U = 3t$. The lower two panels include σ^{reg} for $g = 0$ (dotted lines), i.e. for the pure Hubbard chain. The dashed lines give the normalized integrated spectral weights $S^{reg}(\omega)$. $S^{reg}(\omega)/S^{reg}(\infty)$ with $S^{reg}(\omega) = \int_0^\omega \sigma^{reg}(\omega') d\omega'$ is a natural measure for the relative weight of the different optical absorption processes.

The evolution of the frequency dependence of $\sigma^{reg}(\omega)$ from the PI to the MI phase with increasing U is illustrated in Fig. 3. In the PI regime the electronic excitations are gapped due to the pronounced CDW correlations. The broad optical absorption band for $U = 0$ results from particle-hole excitations across the BI gap which are accompanied by multi-phonon absorption and emission processes. The shape of the absorption band reflects the phonon distribution function in the ground state. Excitonic gap states may occur in the process of structural relaxation. In the MI phase the optical gap is by its nature a correlation gap. The lower panel in Fig. 3 shows clearly that $\sigma(\omega)$ of the HHM in the MI phase is dominated by excitations which can be related to those of the pure Hubbard model. In addition, phononic sidebands appear. More interesting, we found phonon-induced states with low spectral weight within the Mott-Hubbard gap. These states can be viewed as a “fingerprint” of the lower Hubbard band and will be discussed in more details elsewhere [9]. Most notably, in-between the PI and MI phases the optical gap closes at U_{opt} and, due to the selection rules for optical transitions, this necessarily implies a ground state level crossing with a site-parity change. We have explicitly verified that the ground state site parity in the PI phase is $P = +1$ and $P = -1$ in the MI phase. For the HHM on finite rings U_{opt} is identical to the critical point where $S_c(\pi)$ sharply drops. From our conductivity data we found evidence for *only one* critical point in the non-adiabatic region.

This finding is corroborated by the results obtained for the spectral density of single-particle excitations associated with the injection of a spin- σ electron with wave number K (inverse photoemission (IPE))

$$A_{K\sigma}^+(\omega) = \sum_m |\langle \psi_m^{(N_{el}+1)} | c_{K\sigma}^\dagger | \psi_0^{(N_{el})} \rangle|^2 \delta[\omega - (E_m^{(N_{el}+1)} - E_0^{(N_{el})})], \quad (5)$$

and the corresponding quantity for the emission of an electron (photoemission (PE))

$$A_{K\sigma}^-(\omega) = \sum_m |\langle \psi_m^{(N_{el}-1)} | c_{K\sigma} | \psi_0^{(N_{el})} \rangle|^2 \delta[\omega + (E_m^{(N_{el}-1)} - E_0^{(N_{el})})]. \quad (6)$$

Here $|\psi_0^{(N_{el})}\rangle$ is the ground state of the system with N_{el} electrons and $|\psi_m^{(N_{el}\pm 1)}\rangle$ are eigenstates of the $(N_{el}\pm 1)$ -particle system. $E_0^{(N_{el})}$ and $E_m^{(N_{el}\pm 1)}$ are the corresponding energies.

For the half-filled band case ($N_{el} = N$, total $S^z=0$ sector), the single-particle spectral function $A_{K\sigma}(\omega) = A_{K\sigma}^+(\omega) + A_{K\sigma}^-(\omega)$ of the interacting system is gapped at $E_F \forall K$, indicating massive charge excitations across the CDW ($U < U_{opt}$) and Mott-Hubbard ($U > U_{opt}$) gaps in the PI and MI phases [9]. When U approaches the critical value U_{opt} from both below and above, the gap feature vanishes for the Fermi momenta $K_F = \pm\pi/2$. Figure 4 displays the K -resolved IPE and PE spectra at $U = U_{opt}$. One recognizes that the spectral function $A_{K\sigma}(\omega)$ obeys various sum rules. The simplest one,

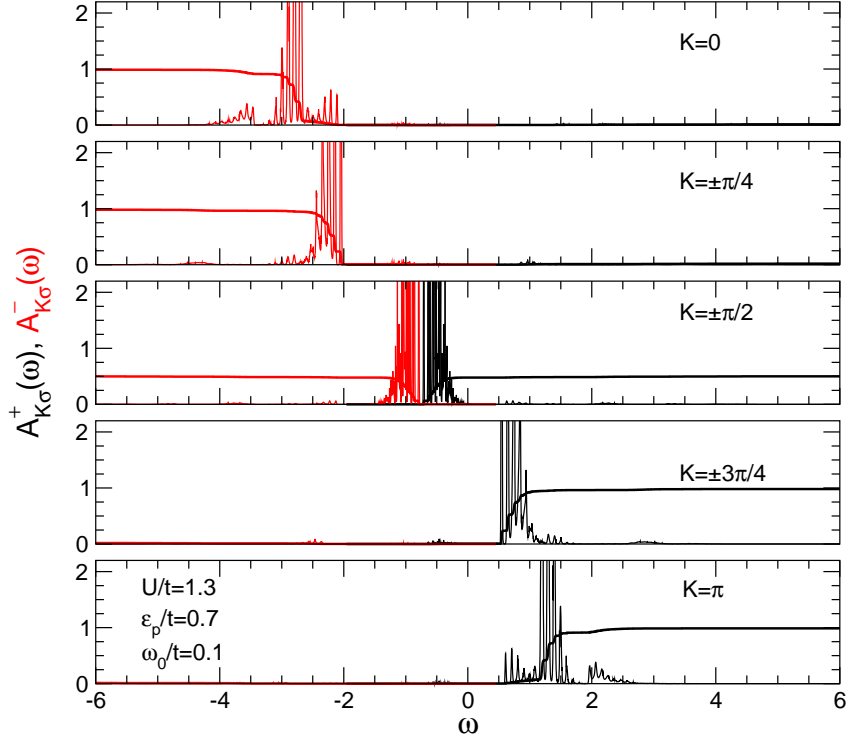


Fig. 4. K -resolved spectral densities (black lines for IPE, red lines for PE) at $U/2\epsilon_p = 0.93$, i.e. in the vicinity of the PI-MI transition point. Included are the integrated spectral weights. Measuring all energies relative to the Fermi energy we note the “particle-hole” symmetry: $A_{K,\sigma}^-(-\bar{\omega}) = A_{\pi-K,\sigma}^+(\bar{\omega})$.

$\int_{-\infty}^{\infty} A_{K\sigma}(\omega)d\omega = 1$, is not useful for (angle-resolved) photoemission spectroscopy (ARPES) since it involves both occupied and unoccupied states [10]. The one-particle density of states is given by $N_{\sigma}(\omega) = \sum_K A_{K\sigma}(\omega)$. The important sum rule for ARPES, however, is $\sum_{\sigma} \int_{-\infty}^{\infty} n_F(\omega) A_{K\sigma}(\omega)d\omega = n(K)$ ($n_F(\omega)$ is the Fermi function), which relates the ARPES intensity to the number of electrons in a momentum state K : $n(K) = \sum_{\sigma} \langle c_{K\sigma}^{\dagger} c_{K\sigma} \rangle$. The momentum distribution $n(K)$ is one for K 's far below K_F and shows a sharp drop for K near K_F .

3 Performance analysis on the Hitachi SR8000-F1

Although there has been a tremendous increase in the computational power during the past decade, the numerical simulation of the interacting quantum systems discussed in the preceding section remains a “grand-challenge application” for modern supercomputers. Even for small clusters, exact diagonal-

ization (ED) studies of microscopic electron-phonon models like the Holstein Hubbard model involve very large sparse matrices. In order to achieve high accuracy within our numerical calculations and to ensure an efficient use of supercomputers DMRG algorithms [11] and *one-step* ED methods (Lanczos [12], Jacobi-Davidson [13], Maximum-Entropy[14]) have been used. The DMRG algorithm which is an iterative method with hundreds of ED steps on a reduced subspace can be run on workstations or multi-processor systems. On the contrary, *one-step* ED techniques require matrix vector multiplications (MVM) involving a sparse matrix representation of the total Hilbert space but provide to date the only method free of any approximations. Since the MVM step determines the computational time as well as the memory requirements for these algorithms, two supplementary MVM strategies have been implemented.

The *in-core* implementation stores the non-zero matrix elements using sparse storage formats, such as *Compressed Row Storage* (CRS) [15] or *Jagged Diagonals Storage* (JDS) [15] yielding high performance at the cost of additional storage. It has been demonstrated [17], that a combination of JDS format (which achieves best performance on vector computers [16]) and an hybrid programming approach is best suited for the Hitachi SR8000-F1, where the 100 GFlop/s barrier can be exceeded on 128 nodes. Furthermore we have shown that, although based on RISC technology, one Hitachi SR8000-F1 node can exceed the performance of comparable present-day vector processors (NEC SX5e) even if vector-gather operations are involved [17]. The *in-core* JDS implementation is used in combination with the Jacobi-Davidson method to compute several low lying eigenstates (10–100) where thousands of MVM steps are required.

A memory-saving, scalable, and parallel algorithm that recomputes the non-zero matrix elements in each MVM step is used for the *out-of-core* MVM implementation (cf. Ref. [7, 18]). In combination with Lanczos (Maximum Entropy) algorithms - which typically need 50–250 MVM steps - the total memory requirements for our ED studies of ground state (spectral) properties can be reduced to approximately 3–4 arrays of the matrix dimension (D_{mat}). Here the available main memory sets the only limit for the matrix dimension accessible for ED and thus determines the quality of our numerical results.

For more than four years the CRAY T3E systems at HLR Stuttgart and NIC Jülich have provided the largest amount of aggregate main memory with a maximum of 128 GB available for production runs. Including the final upgrade at the beginning of 2002 the Hitachi SR8000-F1 system allows us to increase the matrix dimensions by a factor of roughly 7 with approximately 900 GB main memory available for batch jobs on 152 nodes. A brief summary of the development of supercomputers and *out-of-core* MVM implementations used in our ED projects during the past decade is given in Tab. 1. Note that programming language did not change all along, while the parallelization

Table 1. Development of supercomputer resources and programming techniques used for ED in the past decade. System specifications, programming languages and parallelization techniques used in the MVM are given in the first five rows. Maximum matrix sizes achieved on each system and the corresponding time per MVM step are given in the last two rows.

System	TM CM5 GMD St. Augustin	CRAY T3E NIC Jülich	Hitachi SR8000-F1 LRZ Munich
Util. time	1993/1994	1998-	2001-
#CPUs	64	256	1216
Memory	2 GB	128 GB	900 GB
Language	FORTRAN	FORTRAN	FORTRAN
Parallelization	CMFortran	MPI/CRAY-shmem	MPI+OpenMP
$D_{\text{mat}}^{\text{max}}$	5.6×10^7	4.4×10^9	3.3×10^{10}
MVM [s]	156	33	63

strategy of the MVM step had to be adapted several times to ensure the best use of the supercomputer architecture.

Performance and scalability of different *out-of-core* MVM parallelization strategies on the Hitachi SR8000-F1 are depicted in Fig. 5 for a fixed matrix size ($D_{\text{mat}}^{\text{max}} = 1.6 \times 10^9$). Running a pure MPI parallelization (MPP-mode) and

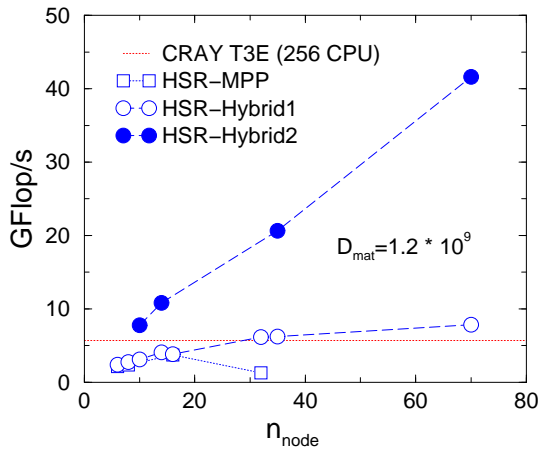


Fig. 5. MVM performance on Hitachi SR8000-F1 (HSR): (i) HSR-MPP: pure MPI mode. (ii) HSR-Hybrid1: Hybrid mode with no additional communication buffer. (iii) HSR-Hybrid2: Hybrid mode with additional communication buffer space. For comparison also MVM performance of a 256 processor CRAY T3E-1200 system is depicted (red line).

assigning one process to each processor, satisfying performance numbers cannot be achieved. At larger processor counts the total performance even drops with increasing number of processors, because a large number of outstanding MPI communication requests over-floods internal message queues. The impact of this bottleneck can be substantially reduced by applying an hybrid programming strategy, where MPI has been used for inter-node communication while shared memory parallelization is carried out within one node (HSR-Hybrid1). As a result, the total number of MPI processes is reduced by a factor of 8 (when compared to the MPP-mode) resulting in performance numbers comparable to CRAY T3E-1200 systems. When spending two additional arrays (of matrix dimension D_{mat}) for buffering of messages and separating communication from computation (HSR-Hybrid2) a performance boost by a factor of 3-4 is obtained. At the same time, however, the maximum matrix dimension achievable by the HSR-Hybrid2 implementation is reduced by a factor of roughly 2 when compared to the HSR-Hybrid1 implementation (cf. Tab. 1).

In conclusion, for the *one-step* ED techniques applied in our project, the hybrid programming approach is the method of choice to achieve high performance and high scalability on the Hitachi SR8000-F1.

4 Conclusions

The work presented in this report is an example for the predictive power of large-scale numerical many-body calculations performed on modern supercomputers. The implementation of the various optimized program packages on the Hitachi SR8000-F1 at the LRZ München allows us to obtain new and exciting insights into the complex interplay of charge, spin, and lattice degrees of freedom in the currently intensively studied quasi-1D materials. More precisely, using quasi-exact numerical techniques to determine the ground state and spectral properties of the one-dimensional half-filled Holstein-Hubbard model, we have revealed the physics behind the crossover from a Peierls band insulator to a correlated Mott-Hubbard insulator. The transition results from a ground state level crossing with a change in the ground state site-parity eigenvalue. In the adiabatic limit, where the quantum phase transition is connected to the band- to Mott-insulator transition of the ionic Hubbard model, two scenarios emerge: a discontinuous PI-MI transition in the strong-coupling regime, and two continuous transitions for weak interactions with an intermediate phase of possible coexistence of charge-density-wave and bond-order-wave. In the non-adiabatic regime, optical conductivity and charge structure factor data indicate that the PI-MI transition proceeds continuously.

Acknowledgements

This work was supported by the *Competence Network for Technical and Scientific High Performance Computing in Bavaria* (KONWIHR, project HQS@HPC) and the Deutsche Forschungsgemeinschaft (project Fe 398-1/2). A. P. K. and M. S. acknowledge support by SFB 484. A. R. B. appreciates the partial support of a Senior Humboldt Fellowship at the University of Bayreuth. Work at Los Alamos is supported by the U.S. D.O.E.

References

1. A. R. Bishop and B. I. Swanson, *Los Alamos Science* **21**, 133 (1993).
2. M. Fabrizio, A. O. Gogolin, and A. A. Nersisyan, *Phys. Rev. Lett.* **83**, 2014 (1999). P. Brune, G.I. Japaridze, and A.P. Kampf, arXiv:cond-mat/0106007. H. Fehske *et al.*, *Physica B* **312-313**, 562 (2002).
3. B. I. Swanson *et al.*, *Phys. Rev. Lett.* **82**, 3288 (1999); *Phys. Rev. Lett.* **82**, 3288 (1999); H. Fehske, M. Kinateder, G. Wellein, and A. R. Bishop, *Phys. Rev. B* **63**, 245121 (2001).
4. N. Gidopoulos, S. Sorella, and E. Tosatti, *Eur. Phys. J. B* **14**, 217 (2000).
5. R. Peierls, *Quantum Theory of Solids* (Oxford University Press, Oxford 1955); R. H. McKenzie and J. W. Wilkins, *Phys. Rev. Lett.* **69**, 1085 (1993); H. Fehske, M. Holicki, and A. Weiße, *Adv. Sol. State Phys.* **40**, 235 (2000).
6. R. J. Bursill, R. H. McKenzie, and C. J. Hamer, *Phys. Rev. Lett.* **80**, 5607 (1998); A. Weiße and H. Fehske, *Phys. Rev. B* **58**, 13526 (1998); E. Jeckelmann, C. Zhang, and S. R. White, *Phys. Rev. B* **60**, 7950 (1999).
7. B. Bäuml, G. Wellein, and H. Fehske, *Phys. Rev. B* **58**, 3663 (1998); A. Weiße, H. Fehske, G. Wellein, and A. R. Bishop, *Phys. Rev. B* **62**, R747 (2000).
8. For a similar conclusion in the IHM see S. Qin, J. Lou, Z. Su, G.-S. Tian, arXiv:cond-mat/0004162v2.
9. H. Fehske *et al.*, to be published.
10. M. Randeria *et al.*, *Phys. Rev. Lett.* **74**, 4951 (1995).
11. S. R. White, *Phys. Rev. B* **48**, 1993 (1993).
12. J. K. Cullum, R. A. Willoughby, *Lanczos Algorithms for Large Symmetric Eigenvalue Computations*, Volumes I & II, Birkhäuser, Boston (1985).
13. G.L.G. Sleijpen and H.A. van der Vorst, *J. Matrix Anal. Appl.* **17**, 401 (1996).
14. R. N. Silver and H. Röder, *Phys. Rev. E* **56**, 4822 (1997).
15. R. Barrett *et al.*, *Templates for the Solution of Linear Systems: Building Blocks for Iterative Methods*, SIAM, Philadelphia (1993).
16. M. Kinateder, G. Wellein, A. Basermann, and H. Fehske, in *High Performance Computing in Science and Engineering '00* edited by E. Krause and W. Jäger, Springer-Verlag, Berlin Heidelberg (2001), pp. 188–204.
17. G. Wellein, G. Hager, A. Basermann, and H. Fehske, *Proceedings of VEC-PAR2002*, Porto (2002).
18. G. Wellein and H. Fehske, in *High Performance Computing in Science and Engineering '99* edited by E. Krause and W. Jäger, Springer-Verlag, Berlin Heidelberg (2000), pp 112-129.